Astronomy & Astrophysics manuscript no. toi118
February 4, 2019

HD 219666 b: a hot-Neptune from *TESS* Sector 1 ⋆

M. Esposito[1], D. J. Armstrong[2,3], D. Gandolfi[4], V. Adibekyan[5], M. Fridlund[6,7], N. C. Santos[5,8], J. H. Livingston[9], E. Delgado Mena[5], L. Fossati[10], J. Lillo-Box[11], O. Barragán[4], D. Barrado[12], P. E. Cubillos[10], B. Cooke[2,3], A. B. Justesen[17], F. Meru[2,3], R. F. Díaz[13,14], F. Dai[22,15], L. D. Nielsen[16], C. M. Persson[6], P. J. Wheatley[2,3], A. P. Hatzes[1], V. Van Eylen[15], M. M. Musso[4], R. Alonso[18,19], P. G. Beck[18,19], S. C. C. Barros[5], D. Bayliss[2,3], A. S. Bonomo[35], F. Bouchy[16], D. J. A. Brown[2,3], E. Bryant[2,3], J. Cabrera[20], W .D. Cochran[21], S. Csizmadia[20], H. Deeg[18,19], O. Demangeon[5], M. Deleuil[23], X. Dumusque[16], P. Eigmüller[20], M. Endl[21], A. Erikson[20], F. Faedi[2,3], P. Figueira[11,5], A. Fukui[24], S. Grziwa[25], E. W. Guenther[1], D. Hidalgo[18,19], M. Hjorth[17], T. Hirano[26], S. Hojjatpanah[5,8], E. Knudstrup[17], J. Korth[25], K. W. F. Lam[28], J. de Leon[9], M. N. Lund[17], R. Luque[18,19], S. Mathur[18,19], P. Montañés Rodríguez[18,19], N. Narita[9,24,29,18,36], D. Nespral[18,19], P. Niraula[27], G. Nowak[18,19], H. P. Osborn[23], E. Pallé[18,19], M. Pätzold[25], D. Pollacco[2,3], J. Prieto-Arranz[18,19], H. Rauer[20,28,31], S. Redfield[30], I. Ribas[32,33], S. G. Sousa[5], A. M. S. Smith[20], M. Tala-Pinto[34], S. Udry[16], and J. N. Winn[15]

(Affiliations can be found after the references)

Received <date> / Accepted <date>

ABSTRACT

We report on the confirmation and mass determination of a transiting planet orbiting the old and inactive G7 dwarf star HD 219666 ($M_\star$=0.92 ± 0.03 $M_\odot$, $R_\star$=1.03 ± 0.03 $R_\odot$, $\tau_\star$=10 ± 2 Gyr). With a mass of M_b = 16.6 ± 1.3 $M_\oplus$, a radius of R_b = 4.71 ± 0.17 $R_\oplus$, and an orbital period of $P_\mathrm{orb} \simeq 6$ days, HD 219666 b is a new member of a rare class of exoplanets: the hot-Neptunes. The Transiting Exoplanet Survey Satellite (*TESS*) observed HD 219666 (also known as TOI-118) in its Sector 1 and the light curve shows four transit-like events, equally spaced in time. We confirmed the planetary nature of the candidate by gathering precise radial velocity measurements with HARPS@ESO 3.6m. We used the co-added HARPS spectrum to derive the host star fundamental parameters (T_eff = 5527 ± 65 K, $\log g_\star$ = 4.40 ± 0.11 (cgs), [Fe/H] = 0.04 ± 0.04 dex, $\log R'_\mathrm{HK} = -5.07 \pm 0.03$), as well as the abundances of many volatile and refractory elements. The host star brightness (V=9.9) makes it suitable for further characterization by means of in-transit spectroscopy. The determination of the planet orbital obliquity, along with the atmospheric metal-to-hydrogen content and thermal structure could provide us with important clues on the mechanisms of formation of this class of objects.

Key words. Planetary systems – Planets and satellites: fundamental parameters – Planets and satellites: individual: HD 219666 b – Stars: fundamental parameters – Techniques: photometric – Techniques: radial velocities

1. Introduction

Following the success of the *Kepler* space mission (Borucki 2016), NASA launched in April 2018 a new satellite, the Transiting Exoplanet Survey Satellite (*TESS*, Ricker et al. 2015). By performing a full-sky survey, *TESS* is expected to detect ∼10 000 transiting exoplanets (TEPs) (Barclay et al. 2018; Huang et al. 2018b). Most interestingly, ∼1000 of them will orbit host stars with magnitude V$\lesssim$10 (as of November 2018 there are 56 known TEPs around stars with V<10, only 13 of which have masses < 20 $M_\oplus$, according to the NASA exoplanet archive[1]). Bright host stars are suitable for precise radial velocity (RV) measurements that can lead to planet mass determinations down to a few $M_\oplus$, and, for TEPs, to estimate the planet bulk density. In-transit precise RVs can also allow us to measure the planet orbital obliquity through the observation of the Rossiter-McLaughlin effect (see, e.g., Triaud 2017). High S/N spectra are very much needed for transmission spectroscopy studies aimed at the detection of atomic and molecular species, and the characterization of the thermal structure of planet atmospheres (Snellen et al. 2010; Bean et al. 2013).

TESS has a field of view of 24° × 96°, and will cover almost the full sky in 26 Sectors, each monitored for about 27 days. Full frame images (FFIs) are registered every 30 minutes, while for a selected sample of bright targets (∼16 000 per Sector) pixel sub-arrays are saved with a 2 minutes cadence. **The first** *TESS* **data set of FFIs from Sectors 1 and 2 was released on December 6th, 2018, and the** *TESS* **Science Office, supported by the Payload Operations Centre at MIT,** had already issued *TESS* data alerts for a number of transiting planet host star candidates, the so called *TESS* Objects of Interest (TOIs). Preliminary 2-min cadence light curves and target pixel files (Twicken et al. 2018) are made publicly available for download at the MAST web site[2].

Several *TESS* confirmed planets have already been announced: π Mensae c (TOI-144), a super-Earth orbiting a V=5.65 mag G0 V star (Huang et al. 2018a; Gandolfi et al. 2018); HD 1397 b (TOI-120), a warm giant planet around a V=7.8 mag sub-giant star (Brahm et al. 2018; Nielsen et al. 2018); HD 2685 b (TOI-135), a hot-Jupiter hosted by an early F-type star (Jones et al. 2018); an ultra-short period Earth-like

⋆ Based on observations made with the 3.6m-ESO telescope at La Silla observatory under ESO programmes IDs 1102.C-0923 (PI: Gandolfi) and 1102.C-0249 (PI: Armstrong).

[1] https://exoplanetarchive.ipac.caltech.edu/.

[2] Mikulski Archive for Space Telescopes, https://archive.stsci.edu/prepds/tess-data-alerts/.

Table 1. Main identifiers, coordinates, parallax, and optical and infrared magnitudes of HD 219666.

Parameter	Value	Source
HD	219666	
TIC ID	266980320	TIC
TOI ID	118	*TESS* Alerts
Gaia DR2 ID	6492940453524576128	*Gaia* DR2[a]
RA (J2000)	$23^h\ 18^m\ 13.630^s$	*Gaia* DR2[a]
DEC (J2000)	-56° 54' 14.036"	*Gaia* DR2[a]
$\mu_{\rm RA}$ [mas yr^{-1}]	313.918 ± 0.039	*Gaia* DR2[a]
$\mu_{\rm DEC}$ [mas yr^{-1}]	-20.177 ± 0.043	*Gaia* DR2[a]
π [mas]	10.590 ± 0.028	*Gaia* DR2[a]
$B_{\rm T}$	10.785 ± 0.027	*Tycho*-2[b]
$V_{\rm T}$	9.897 ± 0.018	*Tycho*-2[b]
G	9.6496 ± 0.0002	*Gaia* DR2[a]
$G_{\rm BP}$	10.0349 ± 0.0009	*Gaia* DR2[a]
$G_{\rm RP}$	9.1331 ± 0.0008	*Gaia* DR2[a]
J	8.557 ± 0.020	2MASS[c]
H	8.254 ± 0.042	2MASS[c]
K_s	8.158 ± 0.033	2MASS[c]
$W1$(3.35 μm)	8.080 ± 0.023	WISE[d]
$W2$(4.6 μm)	8.138 ± 0.020	WISE[d]
$W3$(11.6 μm)	8.100 ± 0.021	WISE[d]
$W4$(22.1 μm)	8.250 ± 0.288	WISE[d]

Notes. [(a)] Gaia Collaboration et al. (2018). [(b)] Høg et al. (2000). [(c)] Cutri et al. (2003). [(d)] Cutri et al. (2013).

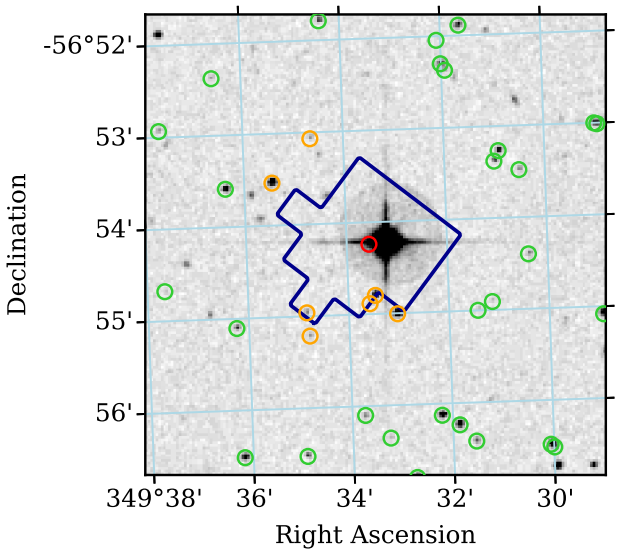

Fig. 1. 5′×5′ archival image taken in 1980 from the SERCJ survey, with the SPOC photometric aperture overplotted in blue (*TESS* pixel size is 21″), and the positions of *Gaia* DR2 sources (J2015.5) within 2′ of HD 219666 indicated by circles. HD 219666 is in red, nearby sources contributing more than 1% of their flux to the aperture are in orange (see Section 2.2), and other sources are in green.

planet around the M dwarf star LHS 3844 (TOI-136; Vanderspek et al. 2018). Here we report on the detection and mass determination of a Neptune-like planet ($M_{\rm b} \simeq 16.6\,M_\oplus$, $R_{\rm b} \simeq 4.7\,R_\oplus$) on a $P_{\rm orb} \simeq$ 6-day orbit around the bright (V=9.9) G7 V star HD 219666 (TOI-118; Table 1).

The work here presented is part of the ongoing RV follow-up effort carried out by two teams, namely, the KESPRINT consortium (see, e.g., Johnson et al. 2016; Van Eylen et al. 2016; Dai et al. 2017; Gandolfi et al. 2017; Barragán et al. 2018; Prieto-Arranz et al. 2018) and the NCORES consortium (see, e.g. Armstrong et al. 2015; Lillo-Box et al. 2016; Barros et al. 2017; Lam et al. 2018; Santerne et al. 2018). Both teams have recently been awarded two large programs with the HARPS spectrograph at the ESO-3.6m telescope to follow-up *TESS* transiting planet candidates. The two consortia have joined forces to make better use of the instrument, optimize the scientific return of the available observing time, and tackle more ambitious planet detections and characterizations.

This paper is organized as follows. Sect. 2 describes the *TESS* photometric data, our custom light curve extraction and assessment of the light contamination factor. Sect. 3 reports on our spectroscopic follow-up observations, which were used to confirm the planetary nature of the transiting companion, and to derive the fundamental parameters and metal abundances of the host star (Sect. 4). The joint analysis of transit light curves and radial velocity data set is described in Sect. 5. Finally we discuss our results in Sect. 6.

2. *TESS* photometry

HD 219666 was observed by *TESS* in Sector 1 (CCD #2 of Camera #2), and falls in a region of the sky that will not be further visited by *TESS*. Sector 1 was monitored continuously for ∼27.9 days, from 2018-07-25 ($\rm BJD_{TDB}$ = 2458325.29953) to 2018-08-22 ($\rm BJD_{TDB}$ = 2458353.17886), with only a 1.14 days gap (from $\rm BJD_{TDB}$ = 2458338.52472 to $\rm BJD_{TDB}$ = 2458339.66500) when the satellite was repointed for data downlink. In addition, between $\rm BJD_{TDB}$ = 2458347 and $\rm BJD_{TDB}$ = 2458350, the *TESS* light curve shows a higher noise level caused by the spacecraft pointing instabilities. The corresponding datapoints were masked out and not included in the analysis presented in this paper.

2.1. Custom light curve preparation

To check that the SPOC aperture is indeed an optimal choice, we extracted a series of light curves from the pixel data using contiguous sets of pixels centered on HD 219666. We first computed the 50$^{\rm th}$ to 95$^{\rm th}$ percentiles (in 1% steps) of the median image, and then selected pixels with median counts above each percentile value to form each aperture. We then computed the 6.5 hour combined differential photometric precision (CDPP) (Christiansen et al. 2012) of the light curve resulting from each of these apertures, and we found that the aperture that minimized the CDPP was slightly larger than the SPOC aperture shown in Fig. 1. However, we opted to use the PDCSAP light curve produced from the SPOC aperture, which has lower levels of systematic noise as a result of the processing performed by the SPOC pipeline (Ricker & Vanderspek 2018).

The median-normalized light curve that we used in our analysis is showed in Fig. 2.

2.2. Limits on photometric contamination

To investigate the possibility of contaminating flux from nearby stars within the SPOC photometric aperture, we compared the *Gaia* DR2 (Gaia Collaboration et al. 2018) sources with the aperture and an archival image of HD 219666 from the SERC-J sur-

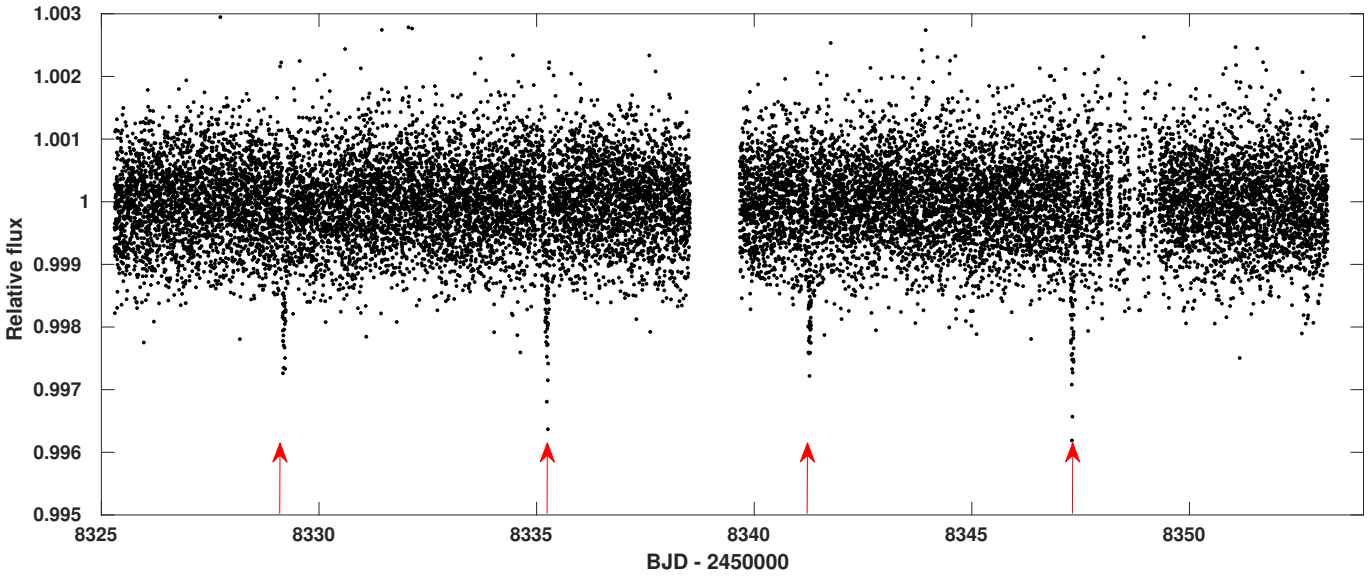

Fig. 2. The *TESS* light curve of HD 219666. The red arrows point to the four planet transit occurrences.

vey[3]. To do so, we executed a query centered on the coordinates of HD 219666 from the *TESS* Input Catalog[4] (TIC; Stassun et al. 2018) using a search radius of 3′. The archival image, taken in 1980, shows HD 219666 to be offset from its current position by ∼4.8″. The proper motion is not sufficient to completely rule out chance alignment with a background source, but such an alignment with a bright source is qualitatively unlikely. We also note the non-detection by *Gaia* of any other sources within ∼30″ of HD 219666. Fig. 1 shows *Gaia* DR2 source positions overplotted on the archival image, along with the SPOC photometric aperture. Using a 2-dimensional Gaussian profile with a FWHM of ∼25″ to approximate the *TESS* point spread function (PSF), and a negligible difference between the $G_{\rm RP}$ and T bandpasses, we found that the transit depth of HD 219666 should be diluted by no more than 0.1%, even considering partial flux contributions from nearby stars outside the aperture. Furthermore, we found that HD 219666 is the only star in or near the aperture that is bright enough to be the source of the transit signal, given the observed depth and assuming a maximum eclipse depth of 100%.

3. HARPS observations

We acquired 21 high-resolution ($R \approx 115\,000$) spectra of HD 219666 with the High Accuracy Radial velocity Planet Searcher (HARPS) spectrograph (Mayor et al. 2003) mounted at the ESO-3.6m telescope of La Silla observatory (Chile). The observations were performed between 02 October and 05 November 2018 UTC, as part of the large observing programmes 1102.C-0923 (PI: Gandolfi) and 1102.C-0249 (PI: Armstrong). We reduced the data using the dedicated HARPS Data Reduction Software (DRS) and extracted the radial velocities (RVs) by cross-correlating the echelle spectra with a G2 numerical mask (Baranne et al. 1996; Pepe et al. 2002; Lovis & Pepe 2007). Table 3 lists the HARPS RVs and their uncertainties, along with the bisector (BIS) and full-width at half maximum (FWHM) of the cross-correlation function (CCF), the Ca II H & K Mount-Wilson S-index, and S/N ratio per pixel at 5500 Å.

The generalized Lomb-Scargle (GLS; Zechmeister & Kürster 2009) periodogram of the HARPS RV measurements (Fig. 3, first panel) shows a significant peak at the frequency of the transit signal ($f_{\rm l} = \mathbf{0.166\ d^{-1}}$; vertical dashed red line), with a false alarm probability[5] (FAP) lower than 0.1 % (horizontal dashed blue line). The peak has no counterpart in the periodograms of the activity indicators, as shown in the second, third, and fourth panels of Fig. 3. This provides strong evidence that the signal detected in our Doppler data is induced by an orbiting companion and confirms the presence of the transiting planet with a period of about 6 days. The periodogram of the RV measurements shows additional peaks symmetrically distributed to the left and right of the dominant frequency. We interpreted these peaks as aliases of the orbital frequency, as shown by the position of the peaks in the periodogram of the window function (Fig. 3, fifth panel).

4. Stellar fundamental parameters

The determination of the stellar parameters from the spectrum of the host star is crucial in order to derive the planetary parameters from transit and radial velocity data. The three most important planetary parameters are the mass, $M_{\rm b}$, the radius $R_{\rm b}$, and the age $\tau_{\rm b}$, all of them only derivable with knowledge of the same parameters for the host star, $M_\star$, $R_\star$, and $\tau_\star$. Therefore we have used two independent methods in order to determine the stellar parameters with the highest degree of confidence available today. For this aim, we utilized the co-added HARPS spectrum, which has a S/N per pixel of ∼300 at 5500 Å.

In one of the methods, we used the Spectroscopy Made Easy code (SME), version 5.22 (Valenti & Piskunov 1996; Valenti & Fischer 2005; Piskunov & Valenti 2017). SME calculates synthetic spectra, utilizing a grid of stellar models, and a set of initial (assumed) fundamental stellar parameters and fits the result to the observed high resolution spectrum with a chi-square minimization procedure. SME contains a large library of differ-

[3] Available at `http://archive.stsci.edu/cgi-bin/dss_form`.
[4] Available at `https://mast.stsci.edu/portal/Mashup/Clients/Mast/Portal.html`.
[5] Computed following the Monte Carlo bootstrap method described in Kuerster et al. (1997).

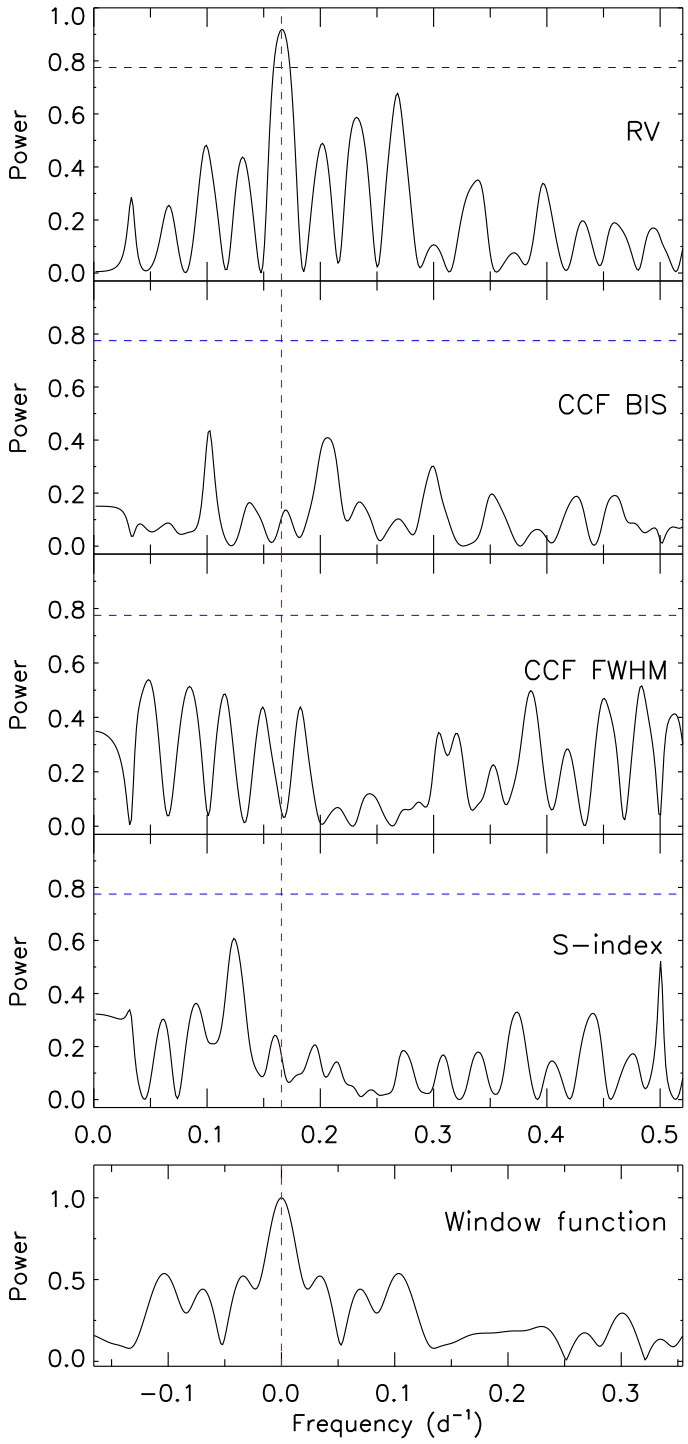

Fig. 3. Generilized Lomb-Scargle periodogram of the HARPS RVs (first panel), of the CCF BIS and FWHM (second and third panel, respectively), of the Ca II H & K S-index (fourth panel), and of the window function (fifth panel). The vertical dashed red line marks the frequency of the transit signal. The horizontal dashed blue line marks the FAP = 0.1% level.

ent 1-D and 3-D model grids. In our analysis of the co-added HD 219666 HARPS spectrum, we used the ATLAS12 model atmosphere grid (Kurucz 2013). This is a set of 1-D models applicable to solar-like stars. The observed spectral features that we fit are sensitive to the different photospheric parameters, including the effective temperature $T_{\rm eff}$, metallicity [M/H], surface gravity $\log g_\star$, micro- and macro-turbulent velocities $v_{\rm mic}$ and $v_{\rm mac}$, and the projected rotational velocity $v \sin i_\star$. In order to minimize the number of free parameters we adopted the calibration equation of Bruntt et al. (2010) to estimate $v_{\rm mic}$ and we fitted many isolated and unblended metal lines to determine $v \sin i_\star$.

We used several different observed spectral features as indicators of each fundamental stellar parameter. The $T_{\rm eff}$ was primarily determined by fitting the wings of Balmer lines, which for solar-type stars are almost totally dependent on the temperature and weakly dependent on gravity and metallicity (Fuhrmann et al. 1993). The surface gravity $\log g_\star$ was determined by fitting the line profiles of the Ca I lines at 6102, 6122, 6162, and 6439 Å, and the profiles of the Mg I triplet at 5160-5185 Å. Results were then checked by fitting also the line wings of the sodium doublet at 5896 and 5890 Å using a sodium abundance determined from a number of fainter lines. In this case all three ions provided the same value for $\log g_\star$. Using this method we derived an effective temperature $T_{\rm eff} = 5450 \pm 70$ K, surface gravity $\log g_\star = 4.35 \pm 0.06$ (cgs), iron content of [Fe/H] = $+0.06 \pm 0.03$ dex, calcium content of [Ca/H] = 0.12 ± 0.05 dex, magnesium [Mg/H] = 0.18 ± 0.10 dex, and sodium [Na/H] = 0.15 ± 0.01 dex. The $v_{\rm mic}$ used was 0.9 ± 0.1 km s^{-1}, and we found $v \sin i_\star = 2.2 \pm 0.8$ km s^{-1} and $v_{\rm mac} = 2.8 \pm 0.9$ km s^{-1}.

In an independent analysis, stellar atmospheric parameters ($T_{\rm eff}$, $\log g_\star$, $v_{\rm mic}$, and [Fe/H]) and respective error bars were derived using the methodology described in Sousa (2014) and Santos et al. (2013). In brief, we made use of the equivalent widths (EW) of 224 Fe I and 35 Fe II lines, as measured in the combined HARPS spectrum of HD 219666 using the ARES v2 code[6] (Sousa et al. 2015), and we assumed ionization and excitation equilibrium. The process makes use of a grid of ATLAS model atmospheres (Kurucz 1993) and the radiative transfer code MOOG (Sneden 1973). As discussed in the references above, this method provides effective temperatures in excellent agreement with values derived using the infra-red flux method that are independent of the derived surface gravity. The resulting values are $T_{\rm eff} = 5527 \pm 25$ K, $\log g_\star = 4.34 \pm 0.04$ (cgs), $v_{\rm mic} = 0.90 \pm 0.04$ km s^{-1}, and [Fe/H] = 0.04 ± 0.02 dex. The surface gravity corrected for the systematic effects discussed in Mortier et al. (2013) has a value of $\log g_\star = 4.40 \pm 0.04$ (cgs).

The two sets of spectroscopic parameters obtained using the two independent methods described above are in good agreement. While we have no reason to prefer one method over the other, in the following analyses we adopted the values derived using the equivalent widths method. We stress that the quoted uncertainties are internal error bars that do not account for the choice of spectral lines and/or atmospheric models. Following Sousa et al. (2011), we accounted for systematic effects by quadratically adding 60 K, 0.1 (cgs), and 0.04 dex to the nominal uncertainty of the effective temperature, surface gravity, and iron content, respectively. The adopted values of $T_{\rm eff} = 5527 \pm 65$ K, $\log g_\star = 4.40 \pm 0.11$ (cgs), and [Fe/H] = 0.04 ± 0.04 dex are listed in Table 2.

Stellar abundances of the elements were also derived using the same tools and models as for stellar parameter determination, as well as using the classical curve-of-growth analysis method, assuming local thermodynamic equilibrium. Although the EWs of the spectral lines were automatically measured with ARES, for the elements with only two-three lines available we performed careful visual inspection of the EWs measurements.

[6] The last version of the ARES code (ARES v2) can be downloaded at `http://www.astro.up.pt/$\sim$sousasag/ares`.

For the derivation of chemical abundances of refractory elements we closely followed the methods described in Adibekyan et al. (e.g. 2012, 2015); Delgado Mena et al. (e.g. 2017). Abundances of the volatile elements, O and C, were derived following the method of Delgado Mena et al. (2010); Bertran de Lis et al. (2015). Since the two spectral lines of oxygen are usually weak and the 6300.3Å line is blended with Ni and CN lines, the EWs of these lines were manually measured with the task `splot` in IRAF. We noticed that for several individual spectra of the star, the 6300Å region was contaminated by the telluric [OI] emission line. We excluded these contaminated spectra when measuring the EW of the stellar oxygen line at 6300.3Å. Lithium and sulfur abundances were derived by performing spectral synthesis with MOOG (Delgado Mena et al. 2014). The final abundances of the elements are presented in Table 2. It is worth noting that the abundances of Na, Mg, and Ca derived with this EW method are in agreement with the abundances obtained with the spectral fitting method. Perhaps it is also interesting to note that the star seems to be enhanced in several α elements (Mg, Si, Ti) and show under-abundance of some heavy elements (e.g. Ba and Y). Such a chemical composition is typical for the so called high-α metal-rich stars first discovered by Adibekyan et al. (2011, 2013). The origin of this population is not fully clear yet, but most probably these stars are migrators from the inner Galaxy (Adibekyan et al. 2011; Anders et al. 2018)

We derived the stellar radius ($R_\star$) combining the *Tycho* B_T, V_T magnitudes, the *Gaia* G, G_{BP}, G_{RP} photometry, and *2MASS* J, H, K_s magnitudes (see Table 1) with our spectroscopic parameters ($T_{\rm eff}$, $\log g_\star$, [Fe/H]; see Table 2) and the *Gaia*' parallax (10.590 ± 0.028 mas, Gaia Collaboration et al. 2018, see Table 2). We corrected the *Gaia* G photometry for the magnitude dependent offset using Eq. 3 from Casagrande & VandenBerg (2018), and adopted a minimum uncertainty of 0.01 mag for the *Gaia* magnitudes to account for additional systematic uncertainties in the *Gaia* photometry. We added 0.06 mas to the nominal *Gaia*'s parallax to account for the systematic offset found by Stassun & Torres (2018), Riess et al. (2018), and Zinn et al. (2018). Following the method described in Gandolfi et al. (2008), we found that the reddening along the line of sight to the star is consistent with zero and did not correct the apparent magnitudes. The bolometric correction for each band-pass was computed using the routine from Casagrande & VandenBerg (2018). We determined a stellar radius of $R_\star = 1.03 \pm 0.03\ R_\odot$.

We used the BAyesian STellar Algorithm (`BASTA`, Silva Aguirre et al. 2015) to determine a stellar mass of $M_* = 0.92 \pm 0.03\ M_\odot$ and an age of $\tau_\star = 10 \pm 2$ Gyr by fitting the stellar radius R_*, effective temperature $T_{\rm eff}$ and iron abundance [Fe/H] to a large, finely-sampled grid of `GARSTEC` stellar models (Weiss & Schlattl 2008).

From the Ca II H & K S-index values provided by the HARPS DRS, we calculated $\log R'_{\rm HK} = -5.07 \pm 0.03$ (Lovis et al. 2011). Using the activity-rotation empirical relationships reported in Noyes et al. (1984) and Mamajek & Hillenbrand (2008), we derived a stellar rotation period of $P_{\rm rot} = 34 \pm 6$ and 37 ± 4 days respectively, which are in good mutual agreement. An upper limit to $P_{\rm rot}$ of 22^{+13}_{-6} days can be inferred from the the stellar radius and $v \sin i_\star$, which is compatible with good alignment between the stellar rotation axis and the planetary orbital axis. We note that the 27.9-day duration of the *TESS* observations is not long enough to attempt a reliable estimation of the photometric stellar rotational period.

Table 2. Fundamental parameters and elemental abundances of HD 219666.

Parameter	Value
Star mass $M_\star$ [$M_\odot$]	0.92 ± 0.03
Star radius $R_\star$ [$R_\odot$]	1.03 ± 0.03
Effective Temperature $T_{\rm eff}$ [K]	5527 ± 65
Surface gravity $\log g_\star$ [cgs]	4.40 ± 0.11
Iron abundance [Fe/H] [dex]	0.04 ± 0.04
Project. rot. vel. $v \sin i_\star$ [km s^{-1}]	2.2 ± 0.8
Micro-turb. vel. $v_{\rm mic}$ [km s^{-1}]	0.9 ± 0.1
Macro-turb. vel. $v_{\rm mac}$ [km s^{-1}]	2.8 ± 0.9
Ca II activity indicator $\log R'_{\rm HK}$	-5.07 ± 0.03
Age $\tau_\star$ [Gyr]	10 ± 2
Lithium abundance A(Li)	<0.40
[C I/H]	0.074±0.065
[O I/H]	0.043±0.148
[Na I/H]	0.090±0.044
[Mg I/H]	0.152±0.049
[Al I/H]	0.196±0.041
[Si I/H]	0.085±0.035
[Ca I/H]	0.041±0.073
[Sc II/H]	0.103±0.050
[Ti I/H]	0.149±0.073
[Ti II/H]	0.097±0.055
[Cr I/H]	0.057±0.055
[Ni I/H]	0.058±0.034
[Cu I/H]	0.148±0.051
[Zn I/H]	0.098±0.038
[Sr I/H]	-0.034±0.105
[Y II/H]	-0.057±0.057
[Zr II/H]	0.027±0.073
[Ba II/H]	-0.058±0.043
[Ce II/H]	0.071±0.063
[Nd II/H]	0.118±0.068
[S I/H]	0.070±0.081

5. Joint analysis of the transit and Doppler data

We performed a joint fit to the *TESS* light curve (Sect. 2) and the 21 HARPS measurements (Sect. 3) utilizing the code `pyaneti` (Barragán et al. 2019). The code uses a Bayesian approach for the model parameter estimations, and samples the posteriors via Markov chain Monte Carlo (MCMC) methods.

We selected 10 hours of photometric data-points centered around each of the four transits observed by *TESS* and flattened the four segments using a second-order polynomial fitted to the out-of-transit data. We fitted the transit light curves using the limb-darkened quadratic model of Mandel & Agol (2002). We set Gaussian priors on the limb darkening coefficients adopting the theoretical values predicted by Claret (2017) along with a conservative error bar of 0.1 for both the linear and the quadratic limb-darkening term. The transit light curve poorly constrains the scaled semi-major axis ($a/R_\star$). We therefore set a Gaussian prior on $a/R_\star$ using the orbital period and the derived stellar parameters (Sec. 4) via Kepler's third law.

The RV model consists of a Keplerian equation. Following (Anderson et al. 2011), we fitted for $\sqrt{e}\sin\omega_\star$ and $\sqrt{e}\cos\omega_\star$, where e is the eccentricity and $\omega_\star$ is the argument of periastron.

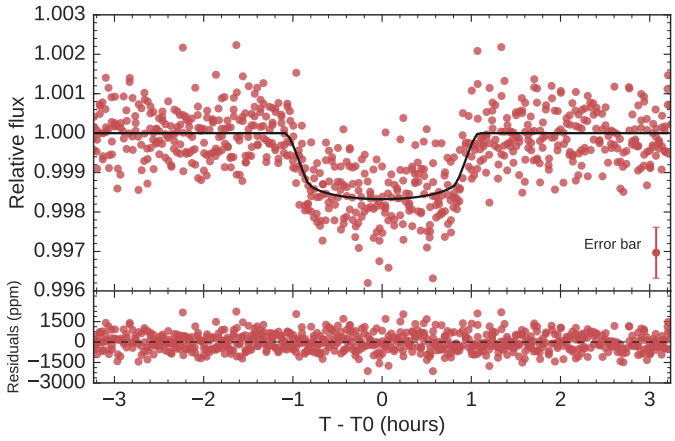

Fig. 4. The phase-folded and normalized *TESS* photometric data with our best fitting transit light curve.

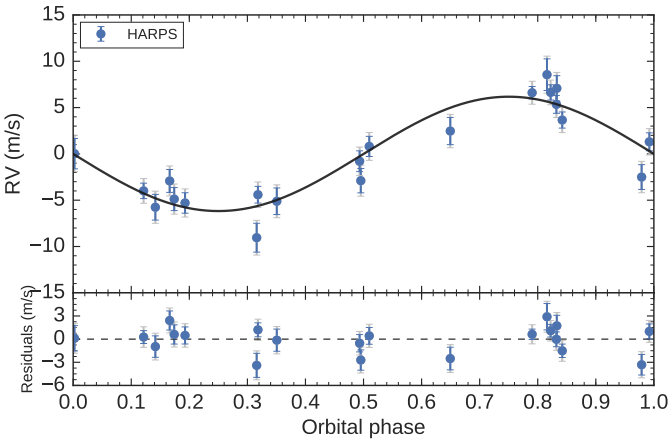

Fig. 5. The phase-folded HARPS RV data points with our best fitting circular RV curve. **The blue error bars correspond to the nominal RV uncertainties calculated by the HARPS DRS while the gray ones account for the RV jitter term. The bottom panel shows the RV residuals that have a rms of 1.7** $\mathrm{m\,s^{-1}}$**.**

We also fitted for an RV jitter term to account for instrumental noise not included in the nominal uncertainties, and/or for RV variations induced by stellar activity. We imposed uniform priors for the remaining fitted parameters. Details of the fitted parameters and prior ranges are given in Table 4.

We used 500 independent Markov chains initialized randomly inside the prior ranges. Once all chains converged, we used the last 5 000 iterations and saved the chain states every ten iterations. This approach generates a posterior distribution of 250 000 points for each fitted parameter. Table 4 lists the inferred planetary parameters. They are defined as the median and 68% region of the credible interval of the posterior distributions for each fitted parameter. The transit and RV curves are shown in Fig. 4 and 5, respectively.

An initial fit for an eccentric orbit yielded $e = 0.07^{+0.06}_{-0.05}$, which is consistent with zero within less than 2σ. We determined the probability that the best-fitting eccentric solution could have arisen by chance if the orbit were actually circular using Monte Carlo simulations. Briefly, we created 10^5 sets of synthetic RVs that sample the best fitting circular solution at the epochs of our observations. We added Gaussian noise at the level of our measurements and fitted the simulated data allowing for an eccentric solution. We found that, given our measurements, there is a 35 % probability that an eccentric solution with $e \geq 0.07$ could have arisen by chance if the orbit were actually circular. As this is above the 5 % significance level suggested by Lucy & Sweeney (1971), we decided to conservatively assume a circular model. We note that the eccentric solution provides a planetary mass that is consistent within less than 1-σ of the result from the circular model.

6. Discussion and conclusion

HD 219666 b has nearly the same mass as Neptune ($M_\mathrm{b} = 16.6 \pm 1.3\ M_\oplus$) but a larger radius ($R_\mathrm{b} = 4.71 \pm 0.17\ R_\oplus$). With an orbital period of $P_\mathrm{orb} \simeq 6$ days and an equilibrium temperature of $T_{eq} \simeq 1073$ K, it is a new member of a relatively rare class of exoplanets: the hot-Neptunes. Fig. 6 shows that HD 219666 b lies in a region of the mass-radius diagram that is scarcely populated. The comparison with rocky planets composition models (Zeng et al. 2016) suggests that HD 219666 b holds a conspicuous gas envelope.

The existence of a hot-Neptunes "desert" was already pointed out (see, e.g., Szabó & Kiss 2011; Mazeh et al. 2016; Owen & Lai 2018), and HD 219666 b falls close to the lower edge of the desert in the mass-period diagram**(see Fig. 1 in Mazeh et al. 2016), and well in the desert in the radius-period diagram (see Fig. 7).** The relative paucity of hot-Neptunes (as compared to hot super-Earths and hot-Jupiters) can be interpreted as a consequence of two different formation mechanisms for short-period planets: in-situ formation for terrestrial planets (Ogihara et al. 2018; Matsumoto & Kokubo 2017), and formation at larger separations followed by inward migration for giant planets (Nelson et al. 2017). Intermediate mass planets like HD 219666 b would then be either the upper tail of terrestrial planets or the lower tail of giant planet distributions. Alternatively giant and small close-in planets could have a common origin but a dramatically different atmospheric escape history (Lundkvist et al. 2016; Ionov et al. 2018; Owen & Lai 2018). **Other mechanisms have been proposed to explain the observed hot-Neptune desert. Matsakos & Königl (2016) advanced an explanation based on high-eccentricity migration followed by tidal circularization. They interpreted the two distinct segments of the desert boundary as a consequence of the different slopes of the empirical mass–radius relation for small and large planets. Batygin et al. (2016) advocated the in-situ formation of close-in super-Earths and hot-Jupiters alike. In the rare cases when a core mass of $M_\mathrm{core} \gtrsim 15 M_\oplus$ would be reached, rapid gas accretion would lead to the formation of a gaseous giant planet. In this way the relative occurrence of Earth- , Neptune- and Jupiter-like close-in planets can be explained.**

To determine whether in situ formation of a planet so close to its star is even possible, we calculate the isolation mass of a planet orbiting with a period of 6 days around a 0.9 $M_\odot$ star. This is the mass of the planet that can form assuming that it grows by consuming all the planetesimals that are within its gravitational influence. Assuming a typical T Tauri disc with a mass of $0.01 M_\odot$ within 100 AU, a gas-to-dust ratio of 100 and a surface mass density profile of $\Sigma \propto R^{-3/2}$ (a steep profile enables as much material as possible to be made available in the inner disc for planet formation), the available rocky material is $\approx 5 \times 10^{-3}\ M_\oplus$. Even if the gas-to-dust ratio was a factor of 10

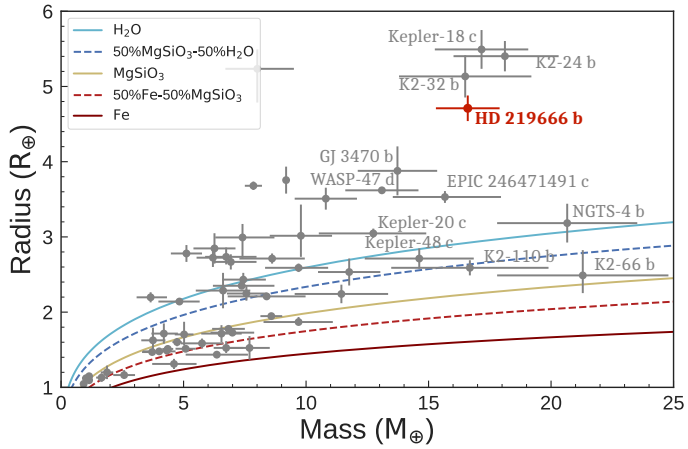

Fig. 6. Mass-radius diagram for planets with masses $M_p < 25\ M_\oplus$ and radii $R_p < 6\ R_\oplus$, as retrieved from the catalogue for transiting planets TEPCat (available at `http://www.astro.keele.ac.uk/jkt/tepcat/`; Southworth 2011). Planets whose masses and radii are known with a precision better than 25% are plotted with grey circles. Composition models from Zeng et al. (2016) are displayed with different lines and colors. The red circle marks the position of HD 219666 b. Planets closer in mass to HD 219666 b are labeled.

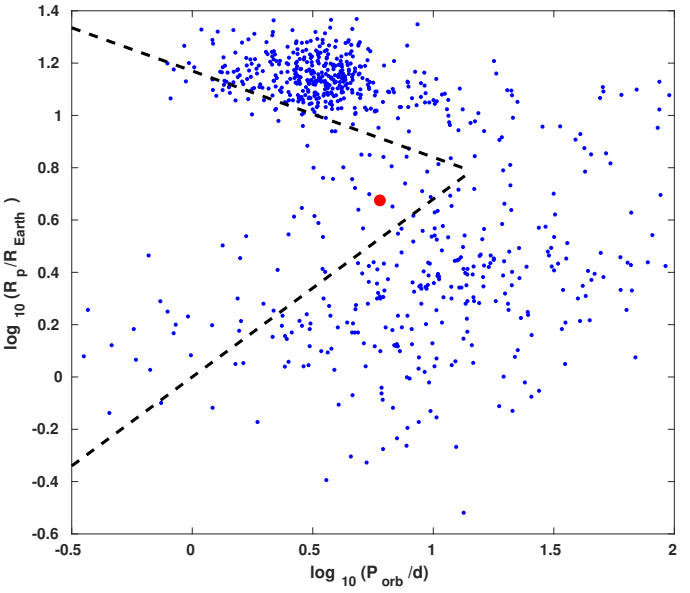

Fig. 7. Planet radius as a function of the orbital period. As for Fig. 6, data are retrieved from TEPCat. The position of HD 219666 b is showed by a red circle. The black dashed lines delimit the hot-Neptunes desert as derived in Mazeh et al. (2016).

lower (Ansdell et al. 2016) the resulting mass is still nowhere near the mass of the planet reported in this study. We point out that this calculation assumes no accretion through the disc when in reality rocky material could drift inwards and build up the core. From the perspective of pebble accretion, Lambrechts et al. (2014) showed that the pebble isolation mass – the core mass at which the drift of pebbles ceases so that the accretion of rocky material onto the core stops – at the radial location of the reported planet is approximately 1 $M_\oplus$, and simulations of planet growth by pebble accretion in evolving discs also show that **an high mass of rocky material cannot be produced in the inner discs (Bitsch et al. 2015). The ~1 $M_\oplus$ upper limit to the rocky material that could have been accreted in-situ has to be compared with an estimate of the M_{core} of HD 219666 b. According to Lopez & Fortney (2014), HD 219666 b, given its mass and radius, should have a H/He envelope which contributes 10 to 20% of its total mass, that is the 80 to 90% of the mass (13 to 15 $M_\oplus$) belongs to the rocky core. Therefore, we conclude that it is more likely that HD 219666 b formed further out and migrated inwards.**

We derived the atmospheric mass-loss rate of HD 219666 b using the interpolation routine presented by Kubyshkina et al. (2018), which is based on a large grid of hydrodynamic upper atmosphere models. The main assumption is that the planet hosts a hydrogen-dominated atmosphere, which, given the measured bulk density, appears to be valid. For the computation, we employed the system parameters listed in Table 2 and a high-energy stellar flux (hereafter called XUV) at the planetary distance to the star of 573.8 erg cm^{-2} s^{-1}, obtained by scaling the solar XUV flux, derived from integrating the solar irradiance reference spectrum (Woods et al. 2009) below 912 Å, to the distance of the planet and the radius of the host star. This is a good assumption because the host star has a mass close to solar and it appears to be rather inactive and old. We obtained a hydrogen mass-loss rate of about 1.2×10^{10} g s^{-1}, which is comparable to what is obtained employing the energy-limited formula (5.2×10^9 g s^{-1}; Erkaev et al. 2007). This indicates that, for this planet, atmospheric expansion and mass loss are driven mostly by atmospheric heating due to absorption of the stellar XUV flux, with an additional component due to the intrinsic thermal energy of the atmosphere and low planetary gravity (Fossati et al. 2017). The obtained mass-loss rate corresponds to 0.06 $M_\oplus$ Gyr^{-1}, suggesting that mass loss does not play a major role in the current evolution of the planetary atmosphere. However, this does not account for the fact that the star was probably more active in the past, particularly during the first few hundred Myr, up to about 1 Gyr (Jackson et al. 2012; Tu et al. 2015), when the XUV fluxes could have been up to about 500 times larger than the current estimate. This would lead to mass-loss rates about 500 times higher. It is therefore likely that atmospheric escape has played a significant role in shaping the early planetary atmospheric evolution.

HD 219666 b is an interesting target for further atmospheric characterization, given its equilibrium temperature of ~1070 K, since the range of expected temperatures at the terminator (depending on the planet's albedo and energy transport) straddles widely different atmospheric chemical compositions under thermochemical equilibrium. Using the properties of the system, we modeled the planet's transmission spectrum using the Python Radiative Transfer in a Bayesian framework[7] (Cubillos et al., in prep.), which is based on the Bayesian Atmospheric Radiative Transfer package (Blecic 2016; Cubillos 2016), and simulated *James Webb Space Telescope (JWST)* observations with Pandexo (Batalha et al. 2017). These models consider opacities from the main spectroscopically active species expected for exoplanets at these wavelengths: H_2O and CO_2 from Rothman et al. (2010); CH_4, NH_3, and HCN from Yurchenko & Tennyson (2014); CO from (Li et al. 2015); Na and K from Burrows et al. (2000); Rayleigh opacities from H, He, and H_2 (Kurucz 1970; Lecavelier Des Etangs et al. 2008); and collision-induced absorption from H_2–H_2 (Borysow et al. 2001; Borysow 2002) and H_2–He (Borysow et al. 1988, 1989; Borysow & Frommhold 1989). We compressed the HITEMP and ExoMol

[7] http://pcubillos.github.io/pyratbay

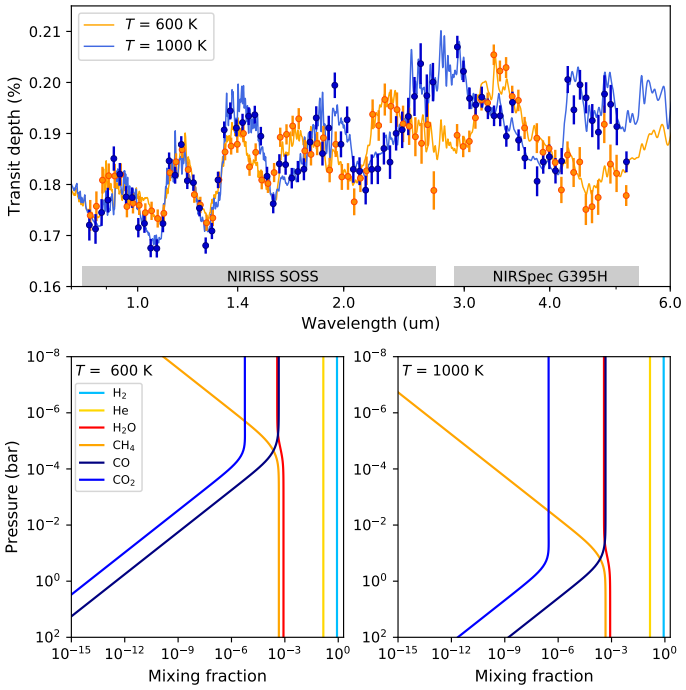

Fig. 8. Model transmission spectra of HD 219666 b (top panel). The dots and error bars denote simulated single-transit *JWST* transmission observations with NIRISS SOSS and NIRSpec G395H (wavelength coverage at bottom) for two underlying models (solid curves) at temperatures of 600 K and 1000 K (see legend). CH_4 shows as strong absorption bands at 1.7, 2.3, and 3.3 μm in the 600 K model; whereas CO and CO_2 show their strongest absorption features at wavelengths beyond 4 μm in the 1000 K model. The bottom panels show the composition of the main species that shape the transmission spectrum. **Depending on the atmospheric temperature, carbon favors either higher CH_4 (temperatures lower than ~900 K) or CO/CO_2 abundances (otherwise).**

databases with the open-source repack package (Cubillos 2017) to extract only the strong, dominating line transitions.

Figure 8 shows estimated transmission spectra of HD 219666 b assuming a cloud-free atmosphere, in thermochemical equilibrium (Blecic et al. 2016) for solar elemental composition, **at two illustrative atmospheric temperatures that lead to different transmission spectra.** By combining NIRISS SOSS and NIRSpec G395H observations, one could potentially constrain the atmospheric chemistry and temperature of the planet with a single-transit observation with each instrument. The transmission spectrum at wavelengths shorter than 2 μm constrain the H_2O abundance for both models, setting the baseline to constrain the abundances of other species. At longer wavelengths, either CH_4 (T = 600 K model) or CO/CO_2 (T = 1000 K model) dominate the carbon chemistry at the probed altitudes (Fig. 8, bottom panels), producing widely different features in the transmission spectrum (Fig. 8, top panel).

An important clue to the formation mechanism of HD 219666 b could come from the knowledge of its orbital obliquity with respect to the stellar equatorial plane, which can be estimated through the observation of the Rossiter-McLaughlin (RM) effect. We calculated that the RV amplitude of the RM effect is of ~3 m s^{-1}, so it would probably be detectable with HARPS, and certainly with ESPRESSO (Pepe et al. 2010). Remarkably, there are only two hot-Neptunes with a reported measure of the orbital obliquity, GJ 436 b (Bourrier et al. 2018) and HAT-P-11 b (Winn et al. 2010), and both have a misaligned orbit .

Given the precise RV measurements from HARPS and the mid-transit time from the TESS mission, we can also constrain the presence of co-orbital planets (or trojans) to HD 219666 b, by putting upper limits to their mass M_t (assuming no other planets in the system or far enough to not perturb the RVs in the time span of our observations). We followed the technique described in Leleu et al. (2017), and subsequently applied in Lillo-Box et al. (2018a,b), to model the RV data by including the so-called α parameter, which accounts for the possible mass imbalance between the L_4 and L_5 regions in the co-orbital region of the planet. α is defined as $M_t/M_b \sin\theta + O(e^2)$, where θ is the resonant angle representing the difference between the mean longitudes of the trojan and the planet. We set Gaussian priors on the time of transit and period of the planet, and left the rest of the parameters (i.e., $e\cos\omega$, $e\sin\omega$, α, γ, and K_b) with uniform broad priors. We also included a slope term and a jitter term to account for white noise. The result of this analysis provides parameters compatible with the prior joint analysis and allows us to set constraints on co-orbital planets in the system. In particular, we find $\alpha = -0.14 \pm 0.22$, which assuming the estimated planet mass provides an upper limit (95% confidence level) of $M_t = 4.6\ M_\oplus$ at L5 and no constraint (i.e. up to the planet's mass) at L4.

In conclusion, we have reported the discovery of a hot-Neptune transiting the bright (V=9.9) G7 V star HD 219666. The collaboration between the `KESPRINT` and `NCORES` consortia has made possible a rapid spectroscopic follow-up with HARPS, leading to the confirmation and characterization of the planet candidate detected by *TESS*. HD 219666 b adds to a list of only five Neptune-like planets ($0.5 < M_p < 2\ M_{Nep}$ with 1 $M_{Nep} = 17.2\ M_\oplus$) transiting a V < 10 star. We have carried out detailed analyses to derive the fundamental parameters and the elemental abundances of the host star. We have discussed the possibility of further characterization of the planet, in particular by examining the potential of *JWST* in-transit observations to detect the presence of molecular features in transmission spectra.

Acknowledgements. **We thank the anonymous referee for her/his useful comments. This paper includes data collected by the TESS mission, which are publicly available from the Mikulski Archive for Space Telescopes (MAST). Funding for the TESS mission is provided by NASA's Science Mission directorate.** ME acknowledges the support of the DFG priority program SPP 1992 "Exploring the Diversity of Extrasolar Planets" (HA 3279/12-1). DB acknowledges support by the Spanish State Research Agency (AEI) Project No. ESP2017-87676-C5-1-R and No. MDM-2017-0737 Unidad de Excelencia "María de Maeztu" - Centro de Astrobiología (INTA-CSIC). DJA gratefully acknowledges support from the STFC via an Ernest Rutherford Fellowship (ST/R00384X/1). This work was supported by FCT - Fundação para a Ciência e a Tecnologia through national funds and by FEDER through COMPETE2020 - Programa Operacional Competitividade e Internacionalização by these grants: UID/FIS/04434/2013 & POCI-01-0145-FEDER-007672; PTDC/FIS-AST/28953/2017 & POCI-01-0145-FEDER-028953 and PTDC/FIS-AST/32113/2017 & POCI-01-0145-FEDER-032113. X.D is grateful to the Branco-Weiss fellowship – Society in Science for its financial support. PJW is supported by the STFC Consolidated Grant ST/P000495/1. S.H. acknowledges support by the fellowships PD/BD/128119/2016 funded by FCT (Portugal). This work has made use of the VALD database, operated at Uppsala University, the Institute of Astronomy RAS in Moscow, and the University of Vienna. This publication makes use of The Data & Analysis Center for Exoplanets (DACE), which is a facility based at the University of Geneva (CH) dedicated to extrasolar planets data visualisation, exchange and analysis. DACE is a platform of the Swiss National Centre of Competence in Research (NCCR) PlanetS, federating the Swiss expertise in Exoplanet research. The DACE platform is available at `https://dace.unige.ch`. We thank the Swiss National Science Foundation (SNSF) and the Geneva University for their continuous support to our planet search programs. This work has been in particular carried out in the frame of the National Centre for Competence in Research "PlanetS" supported by the Swiss National Science Foundation (SNSF). S.C.C.B., N.C.S., S.G.S,

Table 3. HARPS RV measurements of HD 219666.

BJD^a_{TDB} -2450000	RV [km s^{-1}]	σ_{RV} [km s^{-1}]	BIS [km s^{-1}]	FWHM [km s^{-1}]	S-index	$\sigma_{S-index}$	T_{exp} [s]	S/N^b
8394.521096	-20.0909	0.0008	-0.0274	6.9061	0.154	0.001	1200	87.9
8394.641680	-20.0939	0.0009	-0.0281	6.9033	0.152	0.002	1200	85.7
8396.644285	-20.1024	0.0012	-0.0242	6.9048	0.144	0.003	1200	62.5
8396.756848	-20.1029	0.0011	-0.0267	6.9081	0.147	0.003	1200	72.4
8397.501496	-20.1066	0.0016	-0.0274	6.9102	0.143	0.004	1500	50.9
8397.710686	-20.1027	0.0014	-0.0253	6.9070	0.144	0.003	1200	54.2
8398.571357	-20.0984	0.0011	-0.0278	6.9130	0.148	0.002	1200	67.3
8398.671630	-20.0968	0.0011	-0.0264	6.9103	0.144	0.002	1200	70.3
8399.513841	-20.0951	0.0015	-0.0316	6.9114	0.148	0.004	1200	53.4
8401.643664	-20.0975	0.0016	-0.0280	6.9094	0.161	0.006	1200	51.8
8404.619501	-20.1005	0.0013	-0.0295	6.9103	0.145	0.003	1200	59.9
8406.554873	-20.0890	0.0017	-0.0282	6.9095	0.146	0.004	1200	47.3
8406.657043	-20.0905	0.0014	-0.0225	6.9092	0.140	0.003	1200	58.1
8407.538610	-20.1001	0.0013	-0.0242	6.9058	0.144	0.003	1200	58.0
8407.618837	-20.0963	0.0010	-0.0274	6.9078	0.150	0.002	1200	78.3
8408.519940	-20.1033	0.0014	-0.0304	6.9129	0.153	0.003	1200	55.6
8408.668982	-20.1005	0.0012	-0.0285	6.9096	0.145	0.003	1200	64.8
8424.508079	-20.0910	0.0007	-0.0263	6.9102	0.153	0.001	1200	108.7
8424.760122	-20.0922	0.0010	-0.0262	6.9148	0.144	0.003	1200	84.8
8426.505548	-20.1016	0.0008	-0.0236	6.9117	0.153	0.001	1200	86.6
8427.693940	-20.1020	0.0009	-0.0267	6.9079	0.152	0.002	1200	89.2

Notes:
[a] Barycentric Julian dates are given in barycentric dynamical time.
[b] S/N per pixel at 5500 Å.

V.A. and E.D.M. acknowledge support from FCT through Investigador FCT contracts nr. IF/01312/2014/CP1215/CT0004, IF/00169/2012/CP0150/CT0002, IF/00028/2014/CP1215/CT0002, IF/00650/2015/CP1273/CT0001, and IF/00849/2015/CP1273/CT0003. This work is partly supported by JSPS KAKENHI Grant Numbers JP18H01265 and 18H05439, and JST PRESTO Grant Number JPMJPR1775. **PGB acknowledges the support of the MINECO under the fellowship program 'Juan de la Cierva incorporacion' (IJCI-2015-26034).**

References

Adibekyan, V., Figueira, P., Santos, N. C., et al. 2015, A&A, 583, A94
Adibekyan, V. Z., Figueira, P., Santos, N. C., et al. 2013, A&A, 554, A44
Adibekyan, V. Z., Santos, N. C., Sousa, S. G., & Israelian, G. 2011, A&A, 535, L11
Adibekyan, V. Z., Sousa, S. G., Santos, N. C., et al. 2012, A&A, 545, A32
Anders, F., Chiappini, C., Santiago, B. X., et al. 2018, A&A, 619, A125
Anderson, D. R., Collier Cameron, A., Hellier, C., et al. 2011, ApJ, 726, L19
Ansdell, M., Williams, J. P., van der Marel, N., et al. 2016, ApJ, 828, 46
Armstrong, D. J., Santerne, A., Veras, D., et al. 2015, A&A, 582, A33
Baranne, A., Queloz, D., Mayor, M., et al. 1996, A&AS, 119, 373
Barclay, T., Pepper, J., & Quintana, E. V. 2018, ApJS, 239, 2
Barragán, O., Gandolfi, D., & Antoniciello, G. 2019, MNRAS, 482, 1017
Barragán, O., Gandolfi, D., Dai, F., et al. 2018, A&A, 612, A95
Barros, S. C. C., Gosselin, H., Lillo-Box, J., et al. 2017, A&A, 608, A25
Batalha, N. E., Mandell, A., Pontoppidan, K., et al. 2017, PASP, 129, 064501
Batygin, K., Bodenheimer, P. H., & Laughlin, G. P. 2016, ApJ, 829, 114
Bean, J. L., Désert, J.-M., Seifahrt, A., et al. 2013, ApJ, 771, 108
Bertran de Lis, S., Delgado Mena, E., Adibekyan, V. Z., Santos, N. C., & Sousa, S. G. 2015, A&A, 576, A89
Bitsch, B., Lambrechts, M., & Johansen, A. 2015, A&A, 582, A112
Blecic, J. 2016, ArXiv e-prints [arXiv:1604.02692]
Blecic, J., Harrington, J., & Bowman, M. O. 2016, ApJS, 225, 4
Borucki, W. J. 2016, Reports on Progress in Physics, 79, 036901
Borysow, A. 2002, A&A, 390, 779
Borysow, A. & Frommhold, L. 1989, ApJ, 341, 549
Borysow, A., Frommhold, L., & Moraldi, M. 1989, ApJ, 336, 495
Borysow, A., Jorgensen, U. G., & Fu, Y. 2001, J. Quant. Spectr. Rad. Transf., 68, 235
Borysow, J., Frommhold, L., & Birnbaum, G. 1988, ApJ, 326, 509
Bourrier, V., Lovis, C., Beust, H., et al. 2018, Nature, 553, 477
Brahm, R., Espinoza, N., Jordán, A., et al. 2018, ArXiv e-prints [arXiv:1811.02156]
Bruntt, H., Bedding, T. R., Quirion, P.-O., et al. 2010, MNRAS, 405, 1907
Burrows, A., Marley, M. S., & Sharp, C. M. 2000, ApJ, 531, 438
Casagrande, L. & VandenBerg, D. A. 2018, MNRAS, 479, L102
Christiansen, J. L., Jenkins, J. M., Caldwell, D. A., et al. 2012, PASP, 124, 1279
Claret, A. 2017, A&A, 600, A30
Cubillos, P. E. 2016, ArXiv e-prints [arXiv:1604.01320]
Cubillos, P. E. 2017, ApJ, 850, 32
Cutri, R. M., Skrutskie, M. F., van Dyk, S., et al. 2003, 2MASS All Sky Catalog of point sources.
Cutri, R. M., Wright, E. L., Conrow, T., et al. 2013, Explanatory Supplement to the AllWISE Data Release Products, Tech. rep.
Dai, F., Winn, J. N., Gandolfi, D., et al. 2017, AJ, 154, 226
Delgado Mena, E., Israelian, G., González Hernández, J. I., et al. 2010, ApJ, 725, 2349
Delgado Mena, E., Israelian, G., González Hernández, J. I., et al. 2014, A&A, 562, A92
Delgado Mena, E., Tsantaki, M., Adibekyan, V. Z., et al. 2017, A&A, 606, A94
Erkaev, N. V., Kulikov, Y. N., Lammer, H., et al. 2007, A&A, 472, 329
Fossati, L., Erkaev, N. V., Lammer, H., et al. 2017, A&A, 598, A90
Fuhrmann, K., Axer, M., & Gehren, T. 1993, A&A, 271, 451
Gaia Collaboration, Brown, A. G. A., Vallenari, A., et al. 2018, A&A, 616, A1
Gandolfi, D., Alcalá, J. M., Leccia, S., et al. 2008, ApJ, 687, 1303
Gandolfi, D., Barragán, O., Hatzes, A. P., et al. 2017, AJ, 154, 123
Gandolfi, D., Barragán, O., Livingston, J. H., et al. 2018, A&A, 619, L10
Høg, E., Fabricius, C., Makarov, V. V., et al. 2000, A&A, 355, L27
Huang, C. X., Burt, J., Vanderburg, A., et al. 2018a, ArXiv e-prints [arXiv:1809.05967]
Huang, C. X., Shporer, A., Dragomir, D., et al. 2018b, ArXiv e-prints [arXiv:1807.11129]
Ionov, D. E., Pavlyuchenkov, Y. N., & Shematovich, V. I. 2018, MNRAS, 476, 5639
Jackson, A. P., Davis, T. A., & Wheatley, P. J. 2012, MNRAS, 422, 2024
Johnson, M. C., Gandolfi, D., Fridlund, M., et al. 2016, AJ, 151, 171

Table 4. HD 219666 system parameters.

Parameter	Prior[(a)]	Derived value
Model parameters of HD 219666 b		
Orbital period $P_{\rm orb,b}$ (days)	$\mathcal{U}[6.00, 6.08]$	$6.03607^{+0.00064}_{-0.00063}$
Transit epoch $T_{0,\rm b}$ ($\rm BJD_{TDB}-2\,450\,000$)	$\mathcal{U}[8329.10, 8329.30]$	8329.1996 ± 0.0012
Scaled semi-major axis $a_{\rm b}/R_\star$	$\mathcal{N}[14.39, 0.30]$	13.27 ± 0.39
Planet-to-star radius ratio $R_{\rm b}/R_\star$	$\mathcal{U}[0, 0.1]$	0.04192 ± 0.00083
Impact parameter $b_{\rm b}$	$\mathcal{U}[0, 1]$	$0.838^{+0.012}_{-0.013}$
$\sqrt{e}\sin\omega_\star$	$\mathcal{F}[0]$	0
$\sqrt{e}\cos\omega_\star$	$\mathcal{F}[0]$	0
Radial velocity semi-amplitude variation $K_\star$ ($\rm m\,s^{-1}$)	$\mathcal{U}[0, 10]$	6.17 ± 0.46
Additional model parameters		
Parameterized limb-darkening coefficient q_1	$\mathcal{N}[0.34, 0.1]$	0.33 ± 0.10
Parameterized limb-darkening coefficient q_2	$\mathcal{N}[0.23, 0.1]$	0.20 ± 0.10
Systemic velocity $\gamma_{\rm HARPS}$ ($\rm km\,s^{-1}$)	$\mathcal{U}[-20.30, -19.9]$	-20.0976 ± 0.0004
RV jitter term $\sigma_{\rm HARPS}$ ($\rm m\,s^{-1}$)	$\mathcal{U}[0, 100]$	$1.04^{+0.48}_{-0.47}$
Derived parameters of HD 219666 b		
Planet mass $M_{\rm b}$ ($M_\oplus$)	···	16.6 ± 1.3
Planet radius $R_{\rm b}$ ($R_\oplus$)	···	4.71 ± 0.17
Planet mean density $\rho_{\rm b}$ ($\rm g\,cm^{-3}$)	···	$0.87^{+0.12}_{-0.11}$
Semi-major axis of the planetary orbit $a_{\rm b}$ (AU)	···	0.06356 ± 0.00265
Orbit eccentricity $e_{\rm b}$	···	0 (fixed)
Orbit inclination $i_{\rm b}$ (deg)	···	86.38 ± 0.15
Equilibrium temperature[(d)] $T_{\rm eq,\,b}$ (K)	···	1073 ± 20
Transit duration $\tau_{14,\,\rm b}$ (hours)	···	2.158 ± 0.034

Note – [(a)] $\mathcal{U}[a, b]$ refers to uniform priors between a and b, and $\mathcal{F}[a]$ to a fixed a value. [(b)] From spectroscopy and isochrones. [(c)] From spectroscopy. [(d)] Assuming zero albedo and uniform redistribution of heat.

Jones, M. I., Brahm, R., Espinoza, N., et al. 2018, ArXiv e-prints [arXiv:1811.05518]
Kubyshkina, D., Fossati, L., Erkaev, N. V., et al. 2018, ApJ, 866, L18
Kuerster, M., Schmitt, J. H. M. M., Cutispoto, G., & Dennerl, K. 1997, A&A, 320, 831
Kurucz, R. L. 1970, SAO Special Report, 309
Kurucz, R. L. 1993, SYNTHE spectrum synthesis programs and line data
Kurucz, R. L. 2013, ATLAS12: Opacity sampling model atmosphere program, Astrophysics Source Code Library
Lam, K. W. F., Santerne, A., Sousa, S. G., et al. 2018, A&A, 620, A77
Lambrechts, M., Johansen, A., & Morbidelli, A. 2014, A&A, 572, A35
Lecavelier Des Etangs, A., Pont, F., Vidal-Madjar, A., & Sing, D. 2008, A&A, 481, L83
Leleu, A., Robutel, P., Correia, A. C. M., & Lillo-Box, J. 2017, A&A, 599, L7
Li, G., Gordon, I. E., Rothman, L. S., et al. 2015, ApJS, 216, 15
Lillo-Box, J., Barrado, D., Figueira, P., et al. 2018a, A&A, 609, A96
Lillo-Box, J., Demangeon, O., Santerne, A., et al. 2016, A&A, 594, A50
Lillo-Box, J., Leleu, A., Parviainen, H., et al. 2018b, A&A, 618, A42
Lopez, E. D. & Fortney, J. J. 2014, ApJ, 792, 1
Lovis, C., Dumusque, X., Santos, N. C., et al. 2011, ArXiv e-prints [arXiv:1107.5325]
Lovis, C. & Pepe, F. 2007, A&A, 468, 1115
Lucy, L. B. & Sweeney, M. A. 1971, AJ, 76, 544
Lundkvist, M. S., Kjeldsen, H., Albrecht, S., et al. 2016, Nature Communications, 7, 11201
Mamajek, E. E. & Hillenbrand, L. A. 2008, ApJ, 687, 1264
Mandel, K. & Agol, E. 2002, ApJ, 580, L171
Matsakos, T. & Königl, A. 2016, ApJ, 820, L8
Matsumoto, Y. & Kokubo, E. 2017, AJ, 154, 27
Mayor, M., Pepe, F., Queloz, D., et al. 2003, The Messenger, 114, 20
Mazeh, T., Holczer, T., & Faigler, S. 2016, A&A, 589, A75
Mortier, A., Santos, N. C., Sousa, S. G., et al. 2013, A&A, 558, A106
Nelson, B. E., Ford, E. B., & Rasio, F. A. 2017, AJ, 154, 106
Nielsen, L. D., Bouchy, F., Turner, O., et al. 2018, ArXiv e-prints [arXiv:1811.01882]
Noyes, R. W., Hartmann, L. W., Baliunas, S. L., Duncan, D. K., & Vaughan, A. H. 1984, ApJ, 279, 763
Ogihara, M., Kokubo, E., Suzuki, T. K., & Morbidelli, A. 2018, A&A, 615, A63
Owen, J. E. & Lai, D. 2018, MNRAS, 479, 5012
Pepe, F., Mayor, M., Galland, F., et al. 2002, A&A, 388, 632
Pepe, F. A., Cristiani, S., Rebolo Lopez, R., et al. 2010, in Proc. SPIE, Vol. 7735, Ground-based and Airborne Instrumentation for Astronomy III, 77350F
Piskunov, N. & Valenti, J. A. 2017, A&A, 597, A16
Prieto-Arranz, J., Palle, E., Gandolfi, D., et al. 2018, A&A, 618, A116
Ricker, G. & Vanderspek, R. 2018, Data Products From TESS Data Alerts
Ricker, G. R., Winn, J. N., Vanderspek, R., et al. 2015, Journal of Astronomical Telescopes, Instruments, and Systems, 1, 014003
Riess, A. G., Casertano, S., Yuan, W., et al. 2018, ApJ, 861, 126
Rothman, L. S., Gordon, I. E., Barber, R. J., et al. 2010, J. Quant. Spectr. Rad. Transf., 111, 2139
Santerne, A., Brugger, B., Armstrong, D. J., et al. 2018, Nature Astronomy, 2, 393
Santos, N. C., Sousa, S. G., Mortier, A., et al. 2013, A&A, 556, A150
Silva Aguirre, V., Davies, G. R., Basu, S., et al. 2015, MNRAS, 452, 2127
Sneden, C. A. 1973, PhD thesis, THE UNIVERSITY OF TEXAS AT AUSTIN.
Snellen, I. A. G., de Kok, R. J., de Mooij, E. J. W., & Albrecht, S. 2010, Nature, 465, 1049
Sousa, S. G. 2014, [arXiv:1407.5817] [arXiv:1407.5817]
Sousa, S. G., Santos, N. C., Adibekyan, V., Delgado-Mena, E., & Israelian, G. 2015, A&A, 577, A67
Sousa, S. G., Santos, N. C., Israelian, G., et al. 2011, A&A, 526, A99
Southworth, J. 2011, MNRAS, 417, 2166
Stassun, K. G., Oelkers, R. J., Pepper, J., et al. 2018, AJ, 156, 102
Stassun, K. G. & Torres, G. 2018, ApJ, 862, 61

Szabó, G. M. & Kiss, L. L. 2011, ApJ, 727, L44
Triaud, A. H. M. J. 2017, The Rossiter-McLaughlin Effect in Exoplanet Research, 2
Tu, L., Johnstone, C. P., Güdel, M., & Lammer, H. 2015, A&A, 577, L3
Twicken, J. D., Catanzarite, J. H., Clarke, B. D., et al. 2018, PASP, 130, 064502
Valenti, J. A. & Fischer, D. A. 2005, ApJS, 159, 141
Valenti, J. A. & Piskunov, N. 1996, A&AS, 118, 595
Van Eylen, V., Albrecht, S., Gandolfi, D., et al. 2016, AJ, 152, 143
Vanderspek, R., Huang, C. X., Vanderburg, A., et al. 2018, ArXiv e-prints [arXiv:1809.07242]
Weiss, A. & Schlattl, H. 2008, Ap&SS, 316, 99
Winn, J. N., Johnson, J. A., Howard, A. W., et al. 2010, ApJ, 723, L223
Woods, T. N., Chamberlin, P. C., Harder, J. W., et al. 2009, Geophys. Res. Lett., 36, L01101
Yurchenko, S. N. & Tennyson, J. 2014, MNRAS, 440, 1649
Zechmeister, M. & Kürster, M. 2009, A&A, 496, 577
Zeng, L., Sasselov, D. D., & Jacobsen, S. B. 2016, ApJ, 819, 127
Zinn, J. C., Pinsonneault, M. H., Huber, D., & Stello, D. 2018, ArXiv e-prints [arXiv:1805.02650]

[1] Thüringer Landessternwarte Tautenburg, Sternwarte 5, D-07778 Tautenburg, Germany e-mail: mesposito@tls-tautenburg.de
[2] Department of Physics, University of Warwick, Gibbet Hill Road, Coventry, CV4 7AL
[3] Centre for Exoplanets and Habitability, University of Warwick, Gibbet Hill Road, Coventry, CV4 7AL
[4] Dipartimento di Fisica, Università degli Studi di Torino, via Pietro Giuria 1, I-10125, Torino, Italy
[5] Instituto de Astrofísica e Ciências do Espaço, Universidade do Porto, CAUP, Rua das Estrelas, 4150-762 Porto, Portugal
[6] Department of Space, Earth and Environment, Chalmers University of Technology, Onsala Space Observatory, 439 92 Onsala, Sweden
[7] Leiden Observatory, University of Leiden, PO Box 9513, 2300 RA Leiden, The Netherlands
[8] Departamento de Física e Astronomia, Faculdade de Ciencias, Universidade do Porto, Rua Campo Alegre, 4169-007 Porto, Portugal
[9] Department of Astronomy, Graduate School of Science, The University of Tokyo, Hongo 7-3-1, Bunkyo-ku, Tokyo, 113-0033, Japan
[10] Space Research Institute, Austrian Academy of Sciences, Schmiedlstrasse 6, A-8041 Graz, Austria
[11] European Southern Observatory, Alonso de Cordova 3107, Vitacura, Santiago, Chile
[12] Depto. de Astrofísica, Centro de Astrobiología (INTA-CSIC), Campus ESAC (ESA)Camino Bajo del Castillo s/n 28692 Villanueva de la Cañada, Spain
[13] Universidad de Buenos Aires, Facultad de Ciencias Exactas y Naturales. Buenos Aires, Argentina
[14] CONICET - Universidad de Buenos Aires. Instituto de Astronomía y Física del Espacio (IAFE). Buenos Aires, Argentina
[15] Department of Astrophysical Sciences, Princeton University, 4 Ivy Lane, Princeton, NJ, 08544, USA
[16] Geneva Observatory, University of Geneva, Chemin des Mailettes 51, 1290 Versoix, Switzerland
[17] Stellar Astrophysics Centre, Deparment of Physics and Astronomy, Aarhus University, Ny Munkegrade 120, DK-8000 Aarhus C, Denmark
[18] Instituto de Astrofísica de Canarias, C/ Vía Láctea s/n, E-38205, La Laguna, Tenerife, Spain
[19] Departamento de Astrofísica, Universidad de La Laguna, E-38206, Tenerife, Spain
[20] Institute of Planetary Research, German Aerospace Center, Rutherfordstrasse 2, 12489 Berlin, Germany
[21] Department of Astronomy and McDonald Observatory, University of Texas at Austin, 2515 Speedway, Stop C1400, Austin, TX 78712, USA
[22] Department of Physics and Kavli Institute for Astrophysics and Space Research, MIT, Cambridge MA 02139 USA
[23] Aix Marseille Univ, CNRS, CNES, LAM, Marseille, France
[24] National Astronomical Observatory of Japan, NINS, 2-21-1 Osawa, Mitaka, Tokyo 181-8588 Japan
[25] Rheinisches Institut für Umweltforschung an der Universität zu Köln, Aachener Strasse 209, D-50931 Köln Germany
[26] Department of Earth and Planetary Sciences, Tokyo Institute of Technology, Meguro-ku, Tokyo Japan
[27] Department of Earth, Atmospheric and Planetary Sciences, MIT, 77 Massachusetts Avenue, Cambridge, MA 02139
[28] Zentrum für Astronomie und Astrophysik, Technische Universität Berlin, Hardenbergstr. 36 D-10623 Berlin Germany
[29] Astrobiology Center, NINS, 2-21-1 Osawa, Mitaka, Tokyo, 181-8588, Japan
[30] Astronomy Department and Van Vleck Observatory, Wesleyan University, Middletown, CT 06459, USA
[31] Institut für Geologische Wissenschaften, Freie Universität Berlin, Malteserstr. 74–100 D-12249 Berlin Germany
[32] Institut de Ciències de l'Espai (ICE, CSIC), Campus UAB, Bellaterra Spain
[33] Institut d'Estudis Espacials de Catalunya (IEEC), Barcelona, Spain
[34] Landessternwarte Königstuhl, Zentrum für Astronomie der Universität Heidelberg, Königstuhl 12, 69117 Heidelberg, Germany
[35] INAF – Osservatorio Astrofisico di Torino, Via Osservatorio 20, I-10025 Pino Torinese, Italy
[36] JST, PRESTO, 7-3-1 Hongo, Bunkyo-ku, Tokyo, 113-0033, Japan

List of Objects